

Measurement of atmospheric boundary layer based on super-large-scale particle image velocimetry using natural snowfall

M. Toloui · S. Riley · J. Hong · K. Howard ·
L. P. Chamorro · M. Guala · J. Tucker

Received: 13 November 2013/Revised: 19 April 2014/Accepted: 22 April 2014/Published online: 10 May 2014
© Springer-Verlag Berlin Heidelberg 2014

Abstract We present an implementation of super-large-scale particle image velocimetry (SLPIV) to characterize spatially the turbulent atmospheric boundary layer using natural snowfall as flow tracers. The SLPIV technique achieves a measurement area of $\sim 22 \text{ m} \times 52 \text{ m}$, up to 56 m above the ground, with a spatial resolution of $\sim 0.34 \text{ m}$. The traceability of snow particles is estimated based on their settling velocity obtained from the wall-normal component of SLPIV velocity measurements. The results are validated using coincident measurements from sonic anemometers on a meteorological tower situated in close proximity to the SLPIV sampling area. A contrast of the mean velocity and the streamwise Reynolds stress component obtained from the two techniques shows less than 3 and 12 % difference, respectively. Additionally, the turbulent energy spectra measured by SLPIV show a similar inertial subrange and trends when compared to those measured by the sonic anemometers.

1 Introduction

Laboratory studies of near-surface phenomena occurring in the atmospheric boundary layer (ABL) are severely constrained by the enormous differences in Reynolds number associated with the limited range of spatial scales achievable in wind tunnel experiments, and the inability to reproduce the complexities of real-life atmospheric flows. These limitations effectively reduce the relevance of research outcomes to full-scale applications, adversely affecting the study of a wide range of atmospheric fluid mechanics problems, such as pollutant transport above metropolitan areas and the response of civil infrastructure to unsteady forces. Endeavors to furnish detailed flow information are particularly important for the wind energy industry where the size of modern utility-scale wind turbines commonly exceeds 100 m, occupying a significant portion of the ABL. The poor understanding of the aerodynamics around utility-scale turbines and multi-turbine wind power plants drives premature component failure (Musial et al. 2007) and contributes to suboptimal operation at the plant scale with average-rated power losses of 10–20 % (Barthelmie et al. 2009).

The current standard experimental techniques for the assessment of ABL or related atmospheric fluid mechanics problems include single-point measurement methods such as cup and sonic anemometers, and large-scale flow field profilers using reflected light (LiDAR) or sonic waves (SODAR), among others. For example, arrays of sonic anemometers (Hutchins et al. 2012) and hotwire anemometers (Metzger et al. 2007) were utilized to study coherent structures in turbulent boundary layers at very high Reynolds numbers. Nacelle wind measurements, along with meteorological tower data, have been used by Vanderwende and Lundquist (2012) to quantify the effects

M. Toloui · S. Riley · J. Hong · K. Howard ·
L. P. Chamorro · M. Guala · J. Tucker
Saint Anthony Falls Laboratory, 2 Third Avenue, Minneapolis,
MN 55414, USA

M. Toloui · S. Riley · J. Hong (✉)
Department of Mechanical Engineering, University of
Minnesota, 111 Church Street SE, Minneapolis,
MN 55455, USA
e-mail: jhong@umn.edu

K. Howard · M. Guala
Department of Civil Engineering, University of Minnesota,
500 Pillsbury Drive SE, Minneapolis, MN 55455, USA

L. P. Chamorro
Department of Mechanical Science and Engineering, University
of Illinois at Urbana-Champaign, 1206 W. Green St., Urbana,
IL 61801, USA

of atmospheric stability regimes in the boundary layer on turbine power generation. Aitken et al. (2012) examined the ability of LiDAR technology to provide profile measurements of wind speed, direction, and turbulence intensity when impacted by weather conditions such as aerosol backscatter, turbulence, humidity, and precipitation. Barthelmie et al. (2006) focused on the characterization of single turbine wake through the use of SODAR. Similarly, the deployment of two SODARs and a lunar scintillometer allowed for the measurement and evaluation of atmospheric turbulence in mountains by Hickson et al. (2010). Nevertheless, despite providing highly informative flow characterization as shown by many research applications, none of these standard techniques yield a whole-field measurement with sufficient spatial and temporal resolutions to quantify the significant unsteady flow structures that are ubiquitous in the ABL. These structures include, for example, large-scale energetic flow structures in the ABL resulting from various ground covers, as well as a variety of vortical structures in the wake of a turbine, such as blade tip, hub and tower vortices.

Particle image velocimetry (PIV), based on tracking the displacement of tracers in an illuminated flow field, is the most popular non-intrusive measurement technique capable of obtaining planar velocity distributions with the spatio-temporal resolution required to study flow–structure interactions (Adrian 2005). This technique in particular offers valuable and complementary opportunities to advance the characterization of atmospheric fluid mechanics problems. For example, Nakiboğlu et al. (2009) applied the PIV technique in a scaled laboratory setting to measure the velocity field during a study of stack gas dispersion in the ABL, utilizing a field of view (FOV) of approximately $0.3 \times 0.4 \text{ m}^2$ that encompassed the majority of the artificially generated ABL. In comparison, field implementation of PIV to clarify the small-scale spatial structure of the turbulence at the edge of a corn canopy by Van Hout et al. (2007) employed a $0.18 \times 0.18 \text{ m}^2$ FOV, where the height of the FOV ranged from just below the canopy edge to 0.77 m above, detailing only a fraction of the boundary layer in the process. In another turbulent ABL field experiment, Morris et al. (2007) conducted PIV over an FOV of $0.5 \times 1.0 \text{ m}^2$ located at ground level to examine Reynolds number dependence of the structure and statistics of wall-layer turbulence. Thus far, these and other implementations of PIV have not achieved an FOV larger than a few square meters or, when applied within the ABL at full-scale, extended their measurement area beyond the near-ground region, within the lowest 1 % of the boundary layer. In addition, this scale is at least one order of magnitude smaller than what is required for this imaging technique to make an impact in quantifying ABL velocity field or flow–structure interactions for full-scale

applications. Achieving the necessary FOV size requires the solution to many technical challenges that include the high demand for illumination intensity, the generation of a super-large-scale light sheet, and the potentially intrusive effects of a seeding apparatus (Whale et al. 2000). The main obstacle for large-scale PIV measurements in an outdoor non-laboratory environment is the requirement to seed the flow field uniformly and persistently with tracers in an environmentally benign, economic, and non-intrusive fashion. A wide variety of artificially generated flow tracers have been used in large-scale PIV measurement of gas flows, e.g., oil droplets (Adrian et al. 2000), smoke/fog (Van Hout et al. 2007; Morris et al. 2007), and helium-filled soap bubbles (Bosbach et al. 2009). However, for PIV measurement of a super-large FOV ($>100 \text{ m}^2$), it is almost impossible to implement any of these artificial seeding methods.

To overcome this obstacle, we introduce in the current paper a super-large-scale PIV (SLPIV) technique utilizing natural snowfall and its implementation for characterizing turbulent flows in the ABL at the University of Minnesota Eolos Wind Energy Research Field Station in Rosemount, MN. A detailed description of the major considerations in the seeding mechanism using natural snowfall, experiment setup, deployment procedure, and PIV process are presented in Sect. 2. In Sect. 3, we display data from preliminary validation of this technique through a comparison of the mean velocity profile, Reynolds stresses, and energy spectra to point measurement data from an instrumented meteorological tower in immediate proximity to the sampling area of the SLPIV measurements.

2 Experimental setup and analysis

2.1 Tracer particle selection

As mentioned above, it is almost impossible to use any of the artificial seeding methods to achieve PIV measurements in a field of $\sim 100 \text{ m}^2$ scale. Therefore, we have to rely on some natural phenomena to provide long-lasting environmentally benign seeding particles. The natural snowfall, endowed by the unique geographic location of our field site at Minnesota, is utilized as the seeding mechanism in our current research. This approach has the following advantages: (1) natural snowfall involves no economic or environmental cost; (2) it covers a significantly larger region than the entire field station and can thus ensure uniform and persistent particle seeding in our sampling area; (3) snowflakes have strong light scattering capability (especially side scattering) owing to their multifacet crystal structure, which lowers the illumination power required for particle

imaging; (4) using natural snowfall does not involve additional seeding apparatuses (jets, aerial platforms, towers or other structures) to artificially introduce tracers into the sampling area, which can perturb the original flow field.

However, the inertial and gravitational effects of snowflakes impose limitations on their traceability. Libbrecht (2005) discusses how the morphology and density of snow particles can vary substantially according to factors such as relative humidity and temperature. For PIV seeding, it is preferable that the snow particles yield a large surface area and well-defined dendrite structures for strong light scattering yet remain porous and light weight for good traceability. Since snowflakes are generally formed by a number of ice crystals weakly interconnected, the densities of porous snow particles can be more than an order of magnitude smaller than that of the ice. Measurements of fresh snow during snowfalls typically report a mean density in the range of 50–100 kg/m³ (e.g., Kaempfer and Schneebeli 2007; Clifton et al. 2008). Generally, the traceability of snowflakes can be characterized by the Stokes number $St = \tau_p/\tau_f$, where τ_p is the particle response time, and τ_f is a flow time scale, defined as the ratio of a characteristic length scale l to velocity fluctuation u_f of the flow, i.e., l/u_f . For good traceability, the Stokes number should be substantially smaller than 1. The drag coefficient depends on the particle Reynolds number, $Re_p = \rho d|u_f - u_p|/\mu$, where ρ is the fluid density, d is the mean diameter of the particles, u_f and u_p are the fluid and the particle velocity, respectively, and μ is the dynamic viscosity of the fluid. Based on the drag correction factor that Crowe et al. (1998) suggest, the particle response time for a tracer whose density is much greater than the fluid density and $Re_p < 800$ is formulated as $\tau_p = \rho_s d^2/[18 \mu (1 + 0.15 Re_p^{0.687})]$.

During our deployment, we measured the largest extension as the characteristic size of the snowflakes to be within the range of 1 mm to 3 mm by sampling the fresh snowflakes on the ground. In order to estimate the traceability of snowflakes, we approximate them as spherical particles, although we acknowledge the fact that the snowflakes have a more complex morphology, which requires more sophisticated measurements to be determined. The assumption of modeling snowflakes as spheres is employed in other relevant studies on snowflake drag force analysis (e.g., Hanesch 1999). From the measured range of snowflake size, we approximate the snowflakes as spheres of $d = 2$ mm diameter. An estimate of the Stokes number for our experiment using the settling velocity measured by SLPIV is presented in the results Sect. 3.2, which shows reasonably good traceability of snow particles for the large-scale turbulent motions of interest.

2.2 Experimental setup

The field deployment to acquire the data presented here began around midnight on March 5th, 2013, before an upcoming snow storm at the University of Minnesota Eolos Wind Energy Research Field Station in Rosemount, MN. This facility consists of a 2.5 MW Clipper Liberty C96 wind turbine and a 130 m meteorological tower (hereafter referred to as the met tower). The met tower, located 160 m south of the turbine (as south is the predominant wind origin), is designed to characterize the local atmospheric boundary layer. The met tower includes four Campbell Scientific CSAT3 three-dimensional sonic anemometers with 20 Hz sampling rate (located at $z = 10, 30, 80,$ and 129 m) and six cup-and-vane anemometers operating at 1 Hz (located at $z = 7, 27, 52, 77, 102,$ and 126 m). Temperature and relative humidity sensors are also mounted directly on the tower adjacent to the cup-and-vane anemometer booms. Figure 1 illustrates the wind direction and the location of the wind turbine, met tower, and SLPIV experimental setup during the deployment. The SLPIV setup was placed directly adjacent to the met tower where the local meteorological conditions and wind velocity could be accurately determined with the tower sensors. The topography upstream of the measurement plane is a nearly flat field on the scale of 2 km, with a few very sparse roughness elements such as scattered 1–2 story buildings and tree patches. As Manes et al. (2008) discuss, snow coverage can provide additional modulation of the terrain roughness, a consideration applicable to the conditions during our experiment.

The major components in the SLPIV setup (illustrated in Fig. 2) include a light sheet generation system, a high spatial resolution camera mounted on a tripod, and a data acquisition system. The light sheet generation system, shown in Fig. 2a, consists of a 5 kW xenon arc lamp searchlight (Sky Rose model from Grace Stage Lighting) and a curved reflector. The searchlight, powered by Briggs and Stratton 6 kW portable generator, is highly collimated with a divergence less than 0.3° . The beam exiting the searchlight is a disk 300 mm in diameter. Our measurements show that the beam diameter only widens to 600 mm in the first 100 m of its path, which ensures reasonably uniform thickness in both the vertical and horizontal span of our sampling area. The curved reflecting mirror is used to project the beam vertically while expanding it into a light sheet. The expansion angle of the light sheet can be adjusted by controlling the curvature of the reflecting mirror. In our experiment, we limit the expansion angle of the light sheet to 12° in order to concentrate illumination power, thereby extending the vertical span of the SLPIV measurements (Fig. 2b). The entire light system is affixed to a trailer providing good mobility for aligning the light

Fig. 1 **a** A Google map showing the location of the wind turbine, met tower, and SLPIV experimental setup during the deployment on March 5th, 2013. Note that the photographed orientation of the turbine in the Google image does not represent the actual orientation during the deployment. **b** A survey map of the deployment

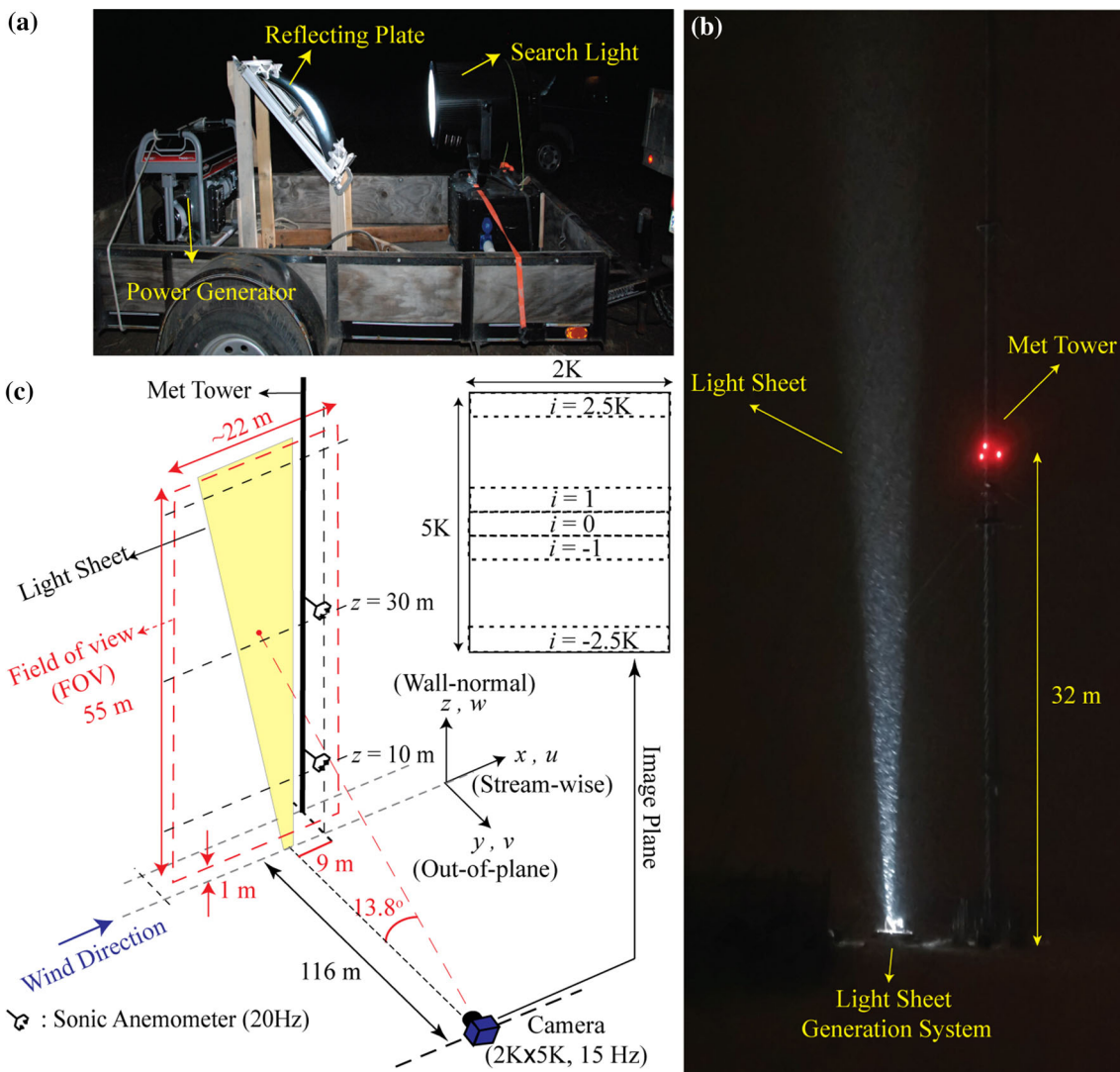
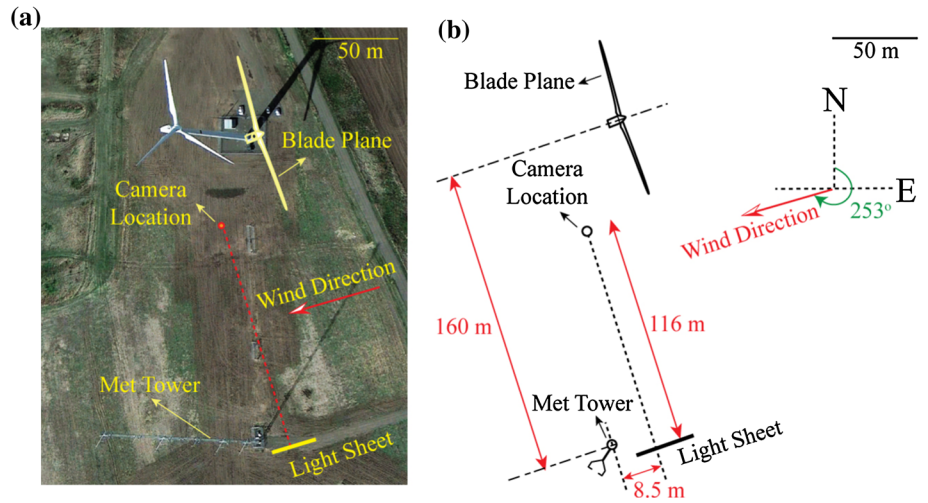


Fig. 2 **a** The setup of the light sheet generation system. **b** A photographic image and **c** a schematic of the experimental setup

sheet in the predominant wind direction to reduce the out-of-plane error as required for planar PIV measurement.

A schematic of the experimental setup is presented in Fig. 2c. The light sheet in the illustration is cutoff at 56 m, which was the maximum height of the SLPIV sampling area limited by the current illumination power and camera sensitivity. The imaging device was a 5 K × 5 K pixel CMOS camera (4.5 μm/pixel) equipped with a 50 mm f/1.2 Nikon lens, with the ability to capture up to 30 frames/s at full sensor size. In this setup, the camera was located 116 m from the light sheet and operated at 15 frames/s with a sensor arrangement of 2 K × 5 K pixels. The numerical aperture on the Nikon lens was adjusted to its upper limit to maximize the light reception of the camera sensor. To reduce blurring created by continuous lighting, the camera shutter speed was set to 45 % of 1/frame rate. Further increase in the shutter speed could result in better imaging of snow particles but was constrained by the lack of illumination power in the upper portion of the viewing field. The optical axis of the camera was in a plane perpendicular to the light sheet and tilted 13.8° from the horizontal. For imaging in a tilt angle, a Scheimpflug adjustment device is used to create a slight angle between the lens plane and camera sensor plane in order to achieve an in-focus image for the entire sampling area. The corresponding depth of field (DOF) for this configuration was calculated to be ~400 mm.

To calibrate our measurements, we first aligned the optical axis perpendicular to the light sheet and level to the ground about its yaw axis, and then measured the tilt angle of the camera (13.8°) and its horizontal distance from the light sheet required to capture the desired field of view. Due to the tilt of the camera, the distances between the lens and the horizontal rows in the FOV at different heights are not the same. For example, the object distance (L_o) for the rows in the upper region of the FOV is longer than that for the rows closer to the bottom (Fig. 2c). This variation in the object distance causes non-uniformity in magnification and consequently non-uniformity in pixel resolution. Based on the focal length of the imaging lens (50 mm) and the object distance for the central row in our FOV, the corresponding image distance from the lens (L_i) is calculated using the thin lens equation ($1/f = 1/L_o + 1/L_i$). Consequently, the magnification ($M_c = L_i/L_c \sim 4.2 \times 10^{-4}$) and the corresponding pixel resolution (i.e., 10.8 mm/pixel) for the central row of the FOV were first calculated to provide the initial estimate of the FOV size. This initial estimate of the pixel resolution was used to determine the object distance for different rows of the FOV. Subsequently, this information was provided for the second iteration of the calibration to correct the magnifications at different heights using $M(i) = L_i(i)/L_o(i)$, where $M(i)$, $L_i(i)$, and $L_o(i)$ are the magnification, the image distance, and the object distance

corresponding to horizontal pixel row number i , respectively, as illustrated in Fig. 2c. The calibration process can be iterated to obtain more accurate pixel resolution by substituting the initial estimate of pixel resolution with the updated pixel resolution calculated from the previous step for object and image distance calculations. However, our test has shown little change of pixel resolution after the second iteration. As a result, the non-uniform pixel resolution at different elevations caused by the tilt angle of the camera, ranges from 10.5 mm/pixel at the lowest height to 11.5 mm/pixel at the highest elevation within the FOV, and the size of the sampling area was determined to be ~22 m × 55 m spanning from 1 to 56 m vertically (see Fig. 2c). The light sheet thickness in the FOV was estimated to be 390 ± 80 mm, close to the ~400 mm DOF of our imaging system. The uncertainty involved in our calibration process includes contributions from both the uncertainty of the horizontal distance measurement (to the camera from the light sheet) and that of the camera tilt angle measurement. According to the specification of our experiment setup and calibration instruments, the maximum light sheet thickness in our FOV (i.e., 470 mm) is the dominant source of the distance measurement uncertainty. The uncertainty of the angle measurement determined by the specification of our angular measurement device is 0.2°. Therefore, the total uncertainty of the calibration process is estimated to be less than 0.06 mm/pixel, corresponding to a maximum uncertainty in the velocity measurement of approximately 0.034 m/s.

Five different SLPIV runs were conducted between 1:27 am and 1:45 am, each containing 34 s of 2 K × 5 K images sampled at 15 Hz (the start and end time for each of these data sets is included in Table 1). The duration of each run was limited by the storage capacity of our acquisition system. The weather and micrometeorological conditions during this period were obtained from the met tower. The temperature stayed between -4.4 °C and -5 °C from 7 to 126 m above the ground with little fluctuation in time. Similarly, the relative humidity remained nearly constant around 98 %. However, from the data provided by sonic anemometers, we observed a discrepancy of predominant wind direction at different elevations, from 253° (clockwise from north) at $z = 10$ m to 278° at $z = 129$ m over the period of our measurement. The light sheet was aligned with the predominant wind direction (253°) measured by the sonic anemometer at the lowest elevation (Fig. 1). During the 1:27–1:45 am period, the bulk Richardson number, estimated as $Ri = gh\Delta T/T_s U_h^2 = -0.07$, indicated that the ABL was weakly unstable; here, the surface temperature T_s was approximated using the temperature measured by the sensor located at 7 m above the ground, $\Delta T \approx 0.5$ K is the mean temperature difference observed along the met tower from 7 to 126 m and U_h is the time-

averaged wind speed at the highest met tower sensor elevation of 129 m.

2.3 Snow PIV image processing

Numerous sources of noise and errors can co-exist for PIV images, including shutter noise, dark noise, diffraction noise, and the nonlinear and non-uniform response of the

camera (Huang et al. 1997). However, the main source of the noise in our experiment was the non-uniform light intensity over the imaging plane, which was caused by light intensity reduction along the light sheet height due to the light absorption by the dense particle field of snowflakes. As illustrated by a sample of a recorded snow particle image in Fig. 3a, the image intensity was drastically reduced with elevation increase, which resulted in lower signal-to-noise ratio (*SNR*) at higher elevations. To quantify the variation in *SNR*, we define $SNR = I_p/I_o$, where I_p and I_o are averaged intensities of the snow particles and the averaged background intensity, respectively, within 32×32 pixel windows at different elevations over the FOV. The *SNR* value of the original SLPIV images was found to drop from 3.7 at $z = 5$ m near the light source to 1.4 at $z = 50$ m near the upper extent of the FOV. As Fig. 3 shows, very near the illumination light source (i.e., $z < \sim 4$ m), the particle images contain highly saturated spots and large particle voids associated with vortical flow

Table 1 Time durations for five PIV runs synchronized with met tower sensors

Data set	Start time	End time
#1	1:27:44 am	1:28:17 am
#2	1:33:18 am	1:33:51 am
#3	1:35:51 am	1:36:24 am
#4	1:37:59 am	1:38:32 am
#5	1:40:29 am	1:41:02 am

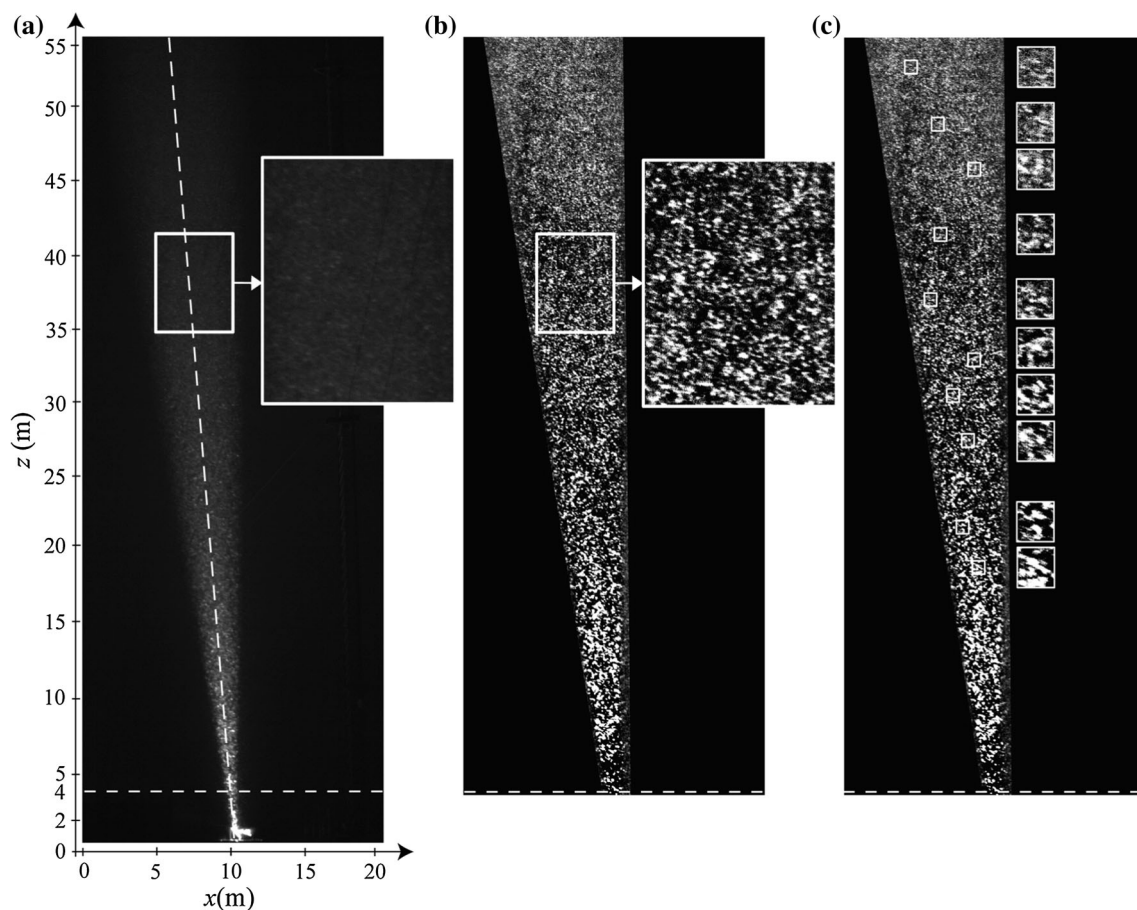


Fig. 3 A sample of **a** the original snow particle image (the *white dot-dashed line* shows the centerline of the illuminated area) and **b** the enhanced particle image after subtraction of time-averaged background and moving local spatial average, and *gray-scale* equalization. A magnified view of a 240×185 pixel window illustrates the effect

of enhancement on the particle image. **c** Magnified particle images in selected 32×32 pixel interrogation windows at different elevations in the enhanced sample image, illustrating the sufficient seeding density for PIV vector calculation

structures generated from the illumination system. Therefore, to ensure valid vector calculations, the PIV cross-correlation was only implemented in the range from $z = 4$ to 56 m.

To achieve accurate PIV vector calculation, the original particle images were enhanced by subtraction of the time-averaged background and moving local spatial average, along with gray-scale equalization. The enhanced version of the PIV image with an enlarged view of a 240×185 pixel window is illustrated in Fig. 3b. The image enhancement algorithm increased the SNR of the original SLPIV images by 2.5 times on average. Figure 3c shows the magnified particle images in randomly selected 32×32 pixel windows at different elevations in the enhanced sample image. As it demonstrates, each window contains 5–7 snow particles, which indicates that the tracer field resulting from natural snowfall is sufficiently homogeneous and dense for implementing PIV vector calculation using a 32×32 pixel interrogation window. The size of snowflakes varies between 6–15 pixels, which are larger than their actual size. In general, the tracer particles appear larger than their true diameters in the particle image of scattered light (Adrian 1991; Adrian and Westerweel 2011). Specifically, the diameter of a tracer particle in the image, d_i , is determined by the particle's scattering diameter d , the imaging magnification (M), and the point response function of the lens. According to Adrian (1991), the diameter of an imaged particle is formulated as, $d_i = (M^2 d^2 + d_s^2)^{1/2}$, where d_s is the diameter increment contributed by diffraction. The d_s is then provided as, $d_s = 2.44(1 + M)f^\# \lambda$, based on the lens f number, $f^\#$, and the wavelength of illumination light source, λ . Moreover, the imaged particles can be larger than this estimate due to various reasons: (1) the complex shape and multifacet characteristics of snowflakes results in greater scattering capability compared with those of spherical particles of the same mass (Matrosov et al. 2005). This reason causes similar discrepancy for sand particles as reported by Zhang et al. (2008). (2) The elongation of the snowflakes along their traveling trajectories associated with the limited shutter speed, which could also contribute to the non-uniformity of the imaged snowflake size at different elevations due to the variation in wind velocity. The non-uniform distribution of imaged snowflake size also has a large contribution from the decreasing illumination at higher elevations as the light propagates through the snow-seeded field due to light absorption and scattering by snowflakes. In addition, the scattering properties of ice crystals-like snowflakes are highly dependent on their orientation (Matrosov 1993; Aydin and Singh 2004), which might also contribute to the variation in particle diameter within our FOV.

The adaptive multi-pass algorithm from LaVision DaVis 7.0 software was employed to calculate the cross-correlation between consecutive image pairs. We applied this algorithm using an initial interrogation window of 128×128 pixels, which was then stepped down to 32×32 pixels with 50 % overlap. This calculation provided a velocity vector field of 0.17 m/vector on average over the sampling area (corresponding to 0.34 m spatial resolution considering 50 % overlap), close to the out-of-plane resolution of our PIV measurements determined by the light sheet thickness or DOF of the imaging system (whichever is smaller). Based on the camera settings and wind conditions during the deployment, the frame-to-frame particle displacement was 15–32 pixels, which is less than 25 % of the initial interrogation window size, satisfying the requirement of the PIV cross correlation algorithm. According to Keane and Adrian (1993) and Adrian and Westerweel (2011), the uncertainty of the vector displacement obtained from PIV 2D cross-correlation is 0.1–0.2 pixels for optimum particle size (2–3 pixels). However, based on the simulation by Raffel et al. (2007) using synthetic particles, this uncertainty rises to 0.3–0.5 pixels for particle sizes of 10–15 pixels using 32×32 interrogation window in PIV cross-correlation calculation. This displacement uncertainty corresponds to a maximum velocity uncertainty of 0.086 m/s in our measurement. It is also noteworthy that the spatial resolution of the current SLPIV measurements corresponds to $\sim 5.2 \times 10^3 l_\nu$, $\sim 240 \eta$ and $\sim 0.016 \delta_\theta$, where l_ν , η , and δ_θ represent the viscous length scale, Kolmogorov scale, and the momentum thickness of the ABL during our experiments, respectively. The viscous length scale is estimated using the friction velocity obtained from a least square log-fit of the mean velocity profile measured by SLPIV (presented in Sect. 3.1). The Kolmogorov scale is calculated to be ~ 1.4 mm from $\eta = (v^3/\varepsilon)^{1/4}$, where v is fluid kinematic viscosity and the dissipation rate, ε is approximated based on the balance between TKE production ($\langle u'w' \rangle du/dz$) and dissipation. This TKE balance is valid for the elevation span of the logarithmic layer in our mean velocity profile (presented in the Sect. 3.1). Note that the estimate of Kolmogorov scale here only offers a crude appreciation of our measurement resolution, which does not consider the uncertainties involved in the calculation of turbulence statistics using PIV data and the fact that planar PIV provides only the in-plane production terms of TKE. The momentum thickness is estimated from the mean velocity profile near ground ($z = 10$ m) up to the highest elevation of the met tower ($z = 129$ m) using the sonic anemometer measurements. As the above discussion shows, our measurements are intended to capture the large scale, energetic turbulent motions in the ABL, not to resolve the full spectrum of turbulence.

3 Results and discussion

In this section, the SLPIV technique using natural snowfall is validated by comparison of the time-averaged streamwise velocity component, Reynolds stress profiles, and turbulent energy spectra from the SLPIV measurements to those obtained from the sonic anemometers within the FOV. Additionally, the wall-normal velocity of the snow particles determined by SLPIV is used to evaluate their flow traceability.

3.1 Mean velocity profile

The previously mentioned variation in the predominant wind direction with height resulted in differing degrees of misalignment between the wind direction and the SLPIV imaging plane within the sample area. The maximum misalignment within the FOV was found to be 13° at $z = 30$ m, which led to an out-of-plane error. This error was estimated as $v \times \Delta t / \Delta z \approx 0.15$, where v is the out-of-plane velocity component, Δt is the time step between consecutive PIV images, and Δz is the light sheet thickness (Keane and Adrian 1993). This maximum error is within the acceptable range for PIV measurements, $v \times \Delta t / \Delta z < 0.25$, according to Keane and Adrian (1993). Nevertheless, to compensate for the misalignment effect, the velocity measured by the sonic anemometers was projected onto the SLPIV imaging plane when compared with the SLPIV measurements. To illustrate the quality of our vector calculations, a sample of the instantaneous velocity field measured by SLPIV is presented in Fig. 4a, b shows a comparison of the mean velocity obtained from these two instruments after the projection. The mean velocity profile from SLPIV was obtained by averaging $\sim 2,500$ vector fields spanning 167 s, which is plotted from $z = 4$ m to $z = 56$ m against the velocity from the two sonic anemometers available in the SLPIV sampling area averaged over the same period. In addition, similar to Hong et al. (2011) the convergence error for mean velocity was estimated using bootstrap analysis, which is implemented by randomly selecting subsamples of 2,000 data points to calculate the statistical distribution of measured mean velocity. The criterion for uncertainty is taken to be twice the standard deviation of the measured statistics distribution, which provides a 95 % level of confidence. As a result, the spatially averaged convergence error over the span of our measurement area for the mean velocity is ~ 0.005 m/s, which is negligible compared to our velocity measurement uncertainty. Note that SLPIV data used for calculating mean velocity and turbulent statistics are only sampled along the centerline of the area covered by the light sheet as shown in Fig. 3a to minimize the effect of deteriorated data quality closer to the edge of the light

sheet. The comparison between the two instruments at corresponding elevations shows less than 3 % difference in the velocity values (2.2 and 2.8 % at $z = 30$ m and $z = 10$ m, respectively). This discrepancy can be contributed by the uncertainties involved in the calibration process, vector calculation of the PIV measurements, and the convergence error since the total contribution of these uncertainties (< 0.13 m/s) is comparable with the maximum difference between sonic and SLPIV measurements (~ 0.1 m/s). Needless to say, this discrepancy can be also affected by the uncertainty associated with sonic anemometers velocity measurement, i.e., 0.08 m/s for each velocity component (provided by the 2012 Campbell Scientific instruction manual).

In a semi-log coordinate system, the mean velocity measured by SLPIV in the range of $z = 6$ – 30 m conforms well to a straight line, which corresponds to a log-layer profile. For fully rough turbulent boundary layer, the mean velocity in the log-layer (neglecting the wake effect term) can be represented as $U^+ = (1/\kappa) \ln(z/z_0)$, where U^+ is the mean streamwise velocity scaled by the friction velocity u^* , the von Karman constant κ is chosen to be 0.41, and z/z_0 is the non-dimensional wall-normal height using the aerodynamic roughness length z_0 (Jiménez 2004). Accordingly, a least square log-fit of SLPIV data from $z = 6$ m to $z = 30$ m resulted in $u^* \approx 0.2$ m/s and $z_0 \approx 0.01$ m, which were used to scale the mean velocity profiles from both SLPIV and sonic anemometers. The results are presented in a semi-log plot in Fig. 4c and show that, below $z = 6$ m ($z/z_0 = 60$), the wind velocity deviates substantially from the log-layer profile. This deviation may be due to the presence of the roughness sublayer, the portion of turbulent boundary layer influenced by surface roughness, existing 2 to 5 h above the ground, where h is the actual height of the roughness element (Raupach et al. 1991). However, according to the topography upstream of our measurement site, it is unlikely that the general upstream terrain could result in the roughness influence of zone extending up to ~ 6 m above the ground. Therefore, we infer that the observed deviation from the logarithmic profile in the surface region of our sampling area is also caused by the local roughness induced by the light-generation system, including the trailer and optical setup (~ 1.5 m in height), and a fence around the base of the met tower, in addition to the nearly homogeneous roughness of the terrain. Moreover, it is noteworthy that, as indicated by the sonic measurements, wind direction varied substantially with elevation during our experiment ($\sim 25^\circ$ between $z = 10$ m and $z = 80$ m). This gradient of wind direction in the atmospheric boundary layer has been described in other studies using meteorological towers (e.g., Handorf et al. 1999; Zilitinkevich et al. 2002; Genthon et al. 2010), and Genthon et al. (2010) claims this phenomenon reflects

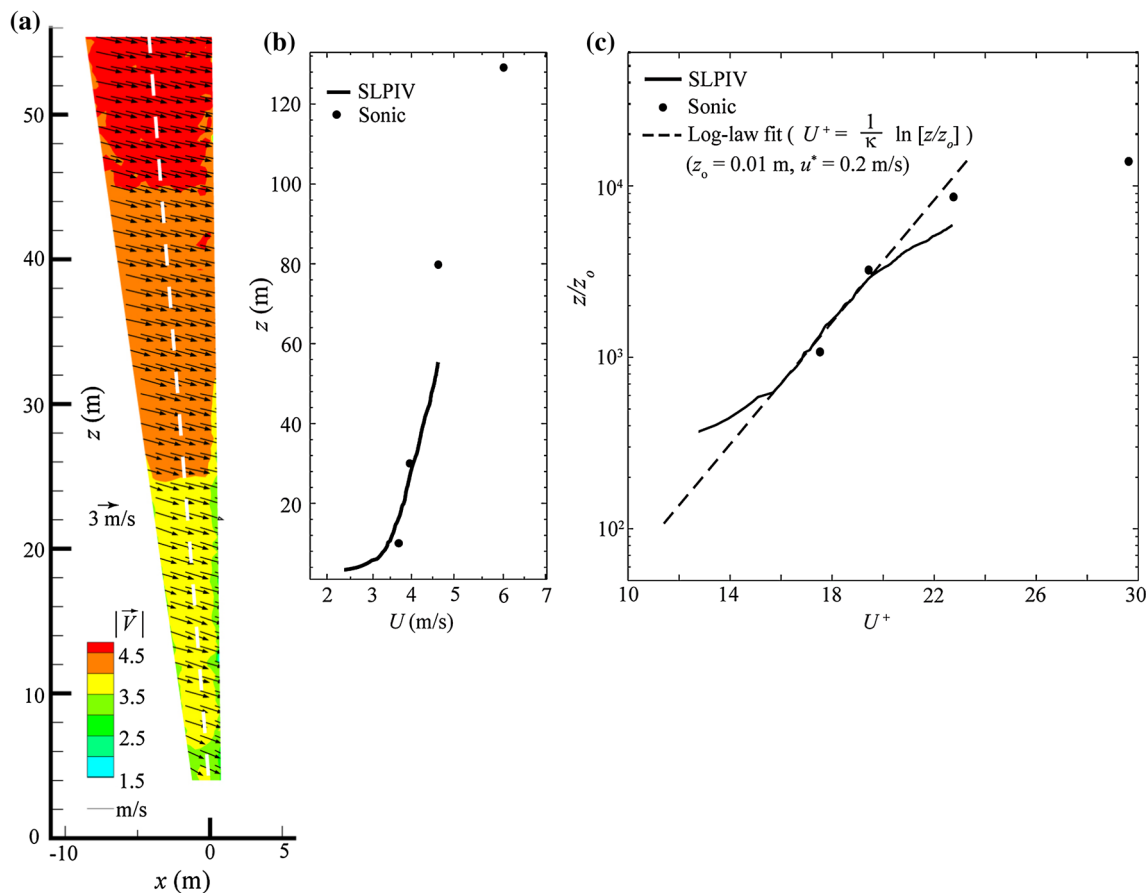


Fig. 4 **a** A sample of an x - z plane instantaneous velocity vector fields from SLPIV measurements superimposed with the contours of the mean velocity magnitude $|\bar{V}|$ (note: the velocity vectors are skipped in 1:3 for clarity). The white dot-dashed line shows the

centerline of the illuminated area. **b** The linear plot and **c** the semi-log plot of the time-averaged streamwise velocity profile measured by SLPIV and sonic anemometers

the lower part of an Ekman spiral. However, none of these prior studies are able to quantify this effect on the logarithmic layer of the mean velocity profile, which could also contribute to the deviation from the log-layer observed in the FOV of our PIV measurements.

3.2 Settling velocity and the traceability of snow particles

The accuracy of PIV measurements depends highly on the ability of flow tracers to follow the turbulent motions at the scales of interest. As mentioned in Sect. 2.1, the traceability of snowflakes can be estimated based on their settling velocity W_s . Here, we obtain the settling velocity of snowflakes by comparing the wall-normal velocity measured with SLPIV to that of the sonic anemometers during our deployment. Figure 5 shows the time-averaged wall-normal velocity within the measurable range of SLPIV ($z = 4$ – 56 m) and the sonic anemometers. The time-averaged wall-normal velocity from SLPIV measurements

varies from -0.8 m/s at $z = 56$ m to -1.2 m/s at $z = 4$ m, with a spatial average value of -1.1 m/s in our sampling area. White et al. (2002) also mentions an increase in snow particles' fall speed as they approach the ground. This increase in snowflake settling velocity can be attributed to various factors including: (1) an increase in snowflake density (Brandes et al. 2007); (2) a change in the shape of the snowflakes to become aerodynamically flattened or tapered during their fall (Jiusto and Bosworth 1971); (3) the sensitivity of the settling velocity of snowflakes to different turbulence levels as they approach the ground (Maahn and Kollias 2012). The increase in density can be caused by a porosity change in the snowflakes or by the temperature gradient as they travel through the air, while the change in shape can be a result of a variation in riming degree or crystal type of the snowflake, or snowflake aggregation. The aggregation of snowflakes is expected during our experiment since the temperature was between -4.4 °C at $z = 7$ m to -4.6 °C at $z = 55$ m within the FOV, which is almost the same as the temperature found by

both Hobbs et al. (1974) of $-5\text{ }^{\circ}\text{C}$ and Hosler et al. (1957) of $-4\text{ }^{\circ}\text{C}$ as the point where the likelihood of snowflakes aggregation escalates due to higher particle stickiness. Comparatively, the wall-normal velocity from sonic measurements stays close to 0 at all the elevations within the FOV. Hence, we estimate the settling velocity of the snow

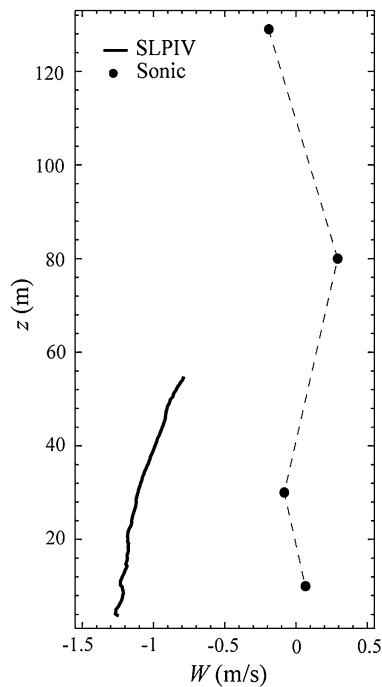


Fig. 5 Time-averaged wall-normal velocity within the measurable range of SLPIV and sonic anemometers

particles to be $W_s \approx 1.1\text{ m/s}$ during the experiment. To compare this value with other studies, a selection of snowflake settling velocity measurements from prior experimental investigations is summarized in Table 2. As it shows, the settling velocity measured by our SLPIV technique is reasonably close to the snow settling velocities predicted by the multiple schemes discussed for unrimed aggregates of thin plates by Mitchell and Heymsfield (2005). The relative increase of ~ 0.2 and $\sim 0.3\text{ m/s}$ in settling velocity from the unmelted/unrimed dendrites to melted and rimed dendrites, respectively, can be clearly observed in measurements by Langleben (1954). In addition, our measurements are within the range of the interrelation of temperature and settling velocity presented by Brandes et al. (2007).

The particle Reynolds number for snowflakes under a spherical shape assumption was estimated to be ~ 178 , which is clearly outside of the Stokes flow regime. Using the drag coefficient corresponding to this Reynolds number regime (Crowe et al. 1998), we obtained the same settling velocity using snow particles of diameter 2 mm with density $\rho_s \approx 52\text{ kg/m}^3$. To achieve an estimate of the turbulence scales captured in our measurements, we make a comparison of the snowflakes to a common PIV tracer, e.g., olive oil droplets ($\rho_s = 970\text{ kg/m}^3$, $d = 3.1\text{ }\mu\text{m}$ from Melling 1997). Under our experimental conditions, the particle response times (τ_p) are $11 \times 10^{-2}\text{ s}$ and $3.24 \times 10^{-5}\text{ s}$ for snowflakes and olive oil droplets, respectively. Therefore, for the same level of traceability, the smallest resolvable turbulence length scale using snowflakes is $\sim 3,400$ times larger than that of the olive oil

Table 2 Selection of snowflake fall speed measurements from other experimental studies

	Size (mm)	Settling velocity (m/s)	Crystal type	T ($^{\circ}\text{C}$)
Langleben (1954)	0.8–2.4 (MD)	0.7–1.0	Dendrites	–2
	0.8–2.4 (MD)	1.1–1.5	Columns and plates	–4
	0.8–2.4 (MD)	0.9–1.2	Melting dendrites	0.5
	0.8–2.4 (MD)	1–1.3	Rimed dendrites	–4
Jiusto and Bosworth (1971)	1–12 (D)	0.7–1.1	Dendritic aggregate	NA
	1–12 (D)	0.9–1.6	Dense snowflakes (plate and column aggregates)	NA
Hanesch (1999)	1–10 (VE)	1.0–1.1	Needles: DOR = 0.4 (unrimed to lightly rimed)	–0.5
	1–10 (VE)	1.1–1.6	Partially melted needles: DOR = 0.7 (lightly rimed)	0
	1–10 (VE)	1.0–1.4	Dendrites: DOR = 1.0 (lightly rimed)	–1
	1–10 (VE)	1.4–1.5	Dendrites and needles: DOR = 1.2 (lightly rimed)	–1.5
	4–8 (VE)	3.1–4.8	Graupel: DOR = 5 (graupel)	–2
Mitchell and Heymsfield (2005)	1–10 (MXD)	0.7–0.9	Unrimed aggregates of thin plates	–5
	1–4 (MXD)	0.3–0.5	Unrimed dendritic crystals	–5
Brandes et al. (2007)	1–11 (EVD)	0.8–1.1	Dendrites, plates, stellars, and their aggregates.	0.1
	1–8 (EVD)	1.0–1.4	Irregular snow particles and lump graupel	–0.5

MD, melted diameter; D, diameter; VE, vertical extension; MXD, maximum diameter; EVD, equivalent volume diameter; DOR, degree of riming

droplets. According to Melling (1997), the olive oil droplets can be employed to resolve turbulent frequencies smaller than 1 kHz ($\tau_f \geq 1 \times 10^{-3}$ s), which corresponds to a turbulence length scale of $l = u_f \times \tau_f = 4 \times 10^{-4}$ m using the maximum value of the root-mean-squared streamwise velocity fluctuations in our sampling area (i.e., $u_f = 0.4$ m/s). Consequently, with the same level of traceability as olive oil droplets capturing turbulent frequencies equal to 1 kHz, snowflakes can trace turbulence length scales above 1.36 m. This length scale, in fact, is fourfold the size of our PIV interrogation window (0.34 m) which imposes another limit on the smallest resolvable turbulence length scale for our measurements. In addition, using a length scale l to be our SLPIV interrogation window size (smallest resolvable length scale regardless of the tracer type) results in $St = 0.13$. Furthermore, a decrease in the Stokes number in accordance with an increasing scale of turbulent structures would suggest a substantial improvement in snow traceability for the large-scale turbulent motions. For instance, to resolve a turbulent eddy of 1 m with a characteristic turbulent velocity scale of 0.4 m/s yields the Stokes number $St = 0.04$, in which case snow particles are deemed acceptable tracers. Finally, the probability density function calculated for velocity fluctuations measured by two sonic anemometers within the FOV shows only 22 % relative likelihood for u' to be more than 0.4 m/s, indicating that the above estimate of the particle traceability is statistically representative for our SLPIV measurements.

3.3 Turbulent statistics

The vertical profiles of three in-plane Reynolds stress components and in-plane turbulent kinetic energy (TKE) measured by SLPIV and the sonic anemometers are presented in Fig. 6. The in-plane Reynolds stresses include the streamwise component $\langle u'u' \rangle$, wall-normal component $\langle w'w' \rangle$, and Reynolds shear stress $\langle u'w' \rangle$. The results from SLPIV measurements yield similar trends as those from sonic anemometers. Using the same bootstrap analysis as explained in Sect. 3.1, the convergence errors (averaged over the elevation span of FOV) are estimated to be $0.004 \text{ m}^2/\text{s}^2$ for $\langle u'u' \rangle$, $0.0016 \text{ m}^2/\text{s}^2$ for $\langle w'w' \rangle$, and $0.0012 \text{ m}^2/\text{s}^2$ for $\langle u'w' \rangle$. The $\langle u'u' \rangle$ obtained from SLPIV have 12 and 5 % difference compared with the corresponding values from sonic measurements at $z = 10$ m and at $z = 30$ m, respectively. These differences are within the convergence error of $\langle u'u' \rangle$ from SLPIV measurements. According to Wilson and Smith (2013), the higher uncertainty at $z = 10$ m as compared to that at $z = 30$ m may be related to the higher velocity gradient and smaller particle displacement near ground.

For $\langle u'w' \rangle$ and $\langle w'w' \rangle$, the deviation between two measurements is above 30 %. Compared with that of $\langle u'u' \rangle$,

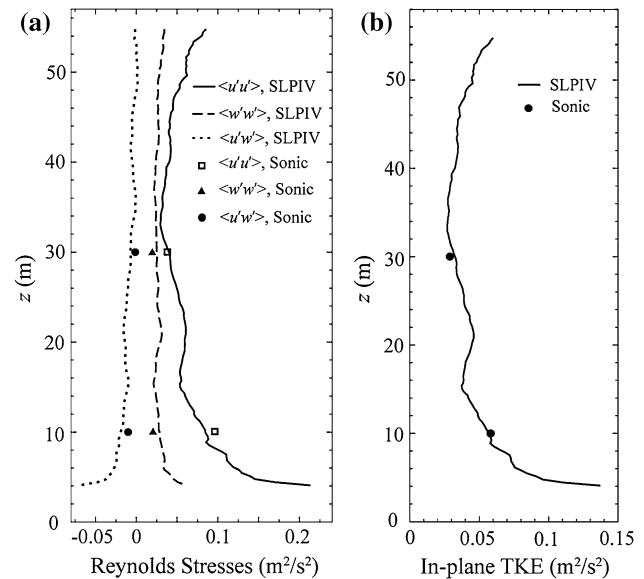
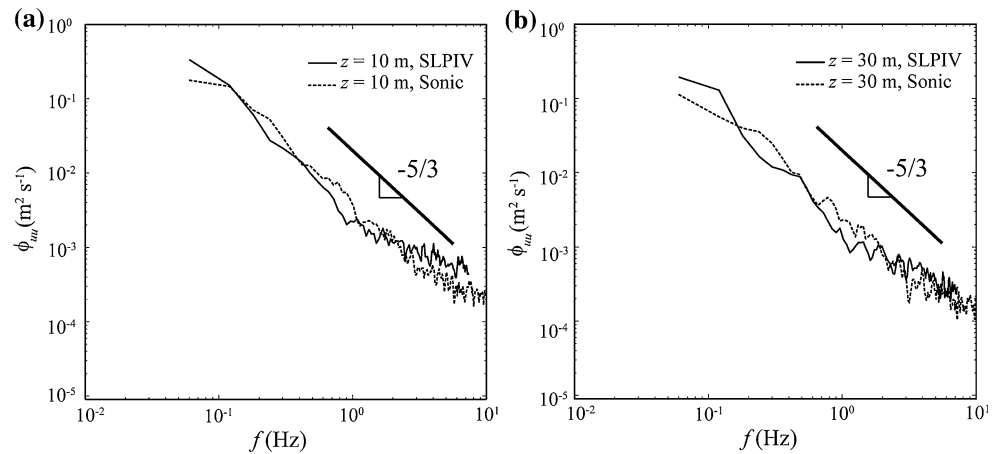


Fig. 6 **a** In-plane Reynolds stress profiles and **b** in-plane turbulent kinetic energy (TKE) profile, in the measurable range of SLPIV compared with the measurements from sonic anemometers at $z = 10$ m and $z = 30$ m

this substantial increase in deviation is primarily related to the significantly smaller wall-normal velocity fluctuations, in which case the relative uncertainty of w' involved in PIV calculation is much larger than that of u' . Note that in the elevation span of $z = 6 - 30$ m, where the mean velocity profile conforms logarithmic law (as illustrated in Fig. 4c), the spatially averaged $\langle u'w' \rangle$ from SLPIV captures ~ 40 % of the u^{*2} in which the u^* is estimated from the mean velocity profile. This result compares favorably with the sonic measured $\langle u'w' \rangle$, which contains only ~ 15 % of u^{*2} . Cautions need to be taken when interpreting the above results. First, as discussed in the Sect. 3.2, the mean velocity profiles from both SLPIV and sonic measurements do not conform to a canonical log-layer profile in the ABL (though there is a logarithmic region). Therefore, the u^{*2} derived from the logarithmic region of the profile may not be an accurate estimate of the Reynolds shear stress $\langle u'w' \rangle$. Second, the deviation of $\langle u'w' \rangle$ and $\langle w'w' \rangle$ between two measurements should be mainly contributed by the uncertainty of the both measurements, rather than the attenuation due to the limited PIV spatial resolution as a number of prior studies state (e.g., Lavoie et al. 2007). This is because the lower spatial resolution of SLPIV associated with a larger interrogation volume (i.e., $0.34 \times 0.34 \times \sim 0.4 \text{ m}^3$ vs. $\sim 3.3 \times 10^{-6} \text{ m}^3$ of the sonics) decreases the magnitude of SPLIV measured Reynolds stresses, while the $\langle w'w' \rangle$ and $\langle u'w' \rangle$ from SLPIV are always higher than those from the sonic anemometers.

As shown in Fig. 6b, the differences of in-plane TKE obtained from both measurements stay within the range of

Fig. 7 Power spectra of the streamwise velocity component measured at **a** $z = 10$ m and **b** $z = 30$ m, by SLPIV and the sonic anemometers



our SLPIV convergence errors, corresponding to 2.5 and 14 % at $z = 10$ m and $z = 30$ m, respectively. The higher discrepancy at $z = 30$ m, as compared to that at the lower elevation, is caused by the fact that the SLPIV measured $\langle w'w' \rangle$ which involves more uncertainty (compared with $\langle u'u' \rangle$) has a larger contribution in TKE at $z = 30$ m.

Figure 7 shows the power spectra of the streamwise velocity component measured by SLPIV and sonic anemometers at $z = 10$ m and at $z = 30$ m, respectively. Evidenced by the classic $-5/3$ slope, the inertial subrange appears in the spectra from both measurements, which further demonstrates the capability of the snow-based SLPIV for turbulence measurements in the ABL. Although the spectra from SLPIV and sonics are close in trend, a clear discrepancy exists. This discrepancy is more likely to be caused by the statistical convergence of the two measurements as opposed to the spatial and temporal attenuation of our SLPIV measurements (i.e., the attenuation associated with slightly lower sampling rate and particle traceability). Limited by the SLPIV acquisition time period, only 167 s data is used to generate the spectra here. In addition, a spectral flattening, i.e., the reduction in spectral slope, occurs at the high frequency range for the SLPIV power spectra. This flattening is an indication of the increased measurement noise level at the high frequency band of SLPIV data (Stanislas et al. 2008).

4 Conclusions

An approach for conducting PIV on a super-large scale using natural snowfall as flow tracers was presented. We implemented this approach to resolve flow statistics in the atmospheric surface layer ranging from 4 to 56 m above the ground with a spatial resolution of ~ 0.34 m and a temporal resolution of 15 Hz. The method was validated by comparing the mean velocity and turbulence statistics with

those obtained from two sonic anemometers instrumented at $z = 10$ m and $z = 30$ m on a met tower, which was located in close proximity to the sampling area of SLPIV. A comparison of mean velocity and the streamwise Reynolds stress component obtained from the two techniques shows less than 3 and 12 % difference, respectively. The SLPIV measured turbulent energy spectra show an inertial subrange and similar trends as compared to those from the sonic measurements.

It should be noted that the current SLPIV implementation is strongly limited by the illumination power of our light sheet generation system, the sampling rate and sensitivity of the imaging camera, as well as the capacity of our data acquisition system. Moreover, it is difficult for the current setup to accommodate the variable conditions in the wind field, resulting in substantial uncertainty associated with the calibration. The envisioned upgrades on the hardware of our current setup, however, should allow further improvement on: (1) the extent of the sampling area of SLPIV; (2) the ability to accommodate high wind speed; (3) the quality of snow particle images; and (4) the accuracy of PIV vector calculation and statistical convergence of our turbulence measurements, etc.

The SLPIV technique introduced in the current paper opens an opportunity to measure super-large-scale flow fields with sufficient spatial and temporal resolution to quantify mean and fluctuating flows in the ABL. This capability can help the study of a number of atmospheric problems including local meteorological phenomena and the response of civil infrastructure (e.g., bridges, highway overpasses, high-rise buildings, etc.) to unsteady forces induced by atmospheric turbulence. In particular, the implementation of SLPIV around utility-scale wind turbines can provide benchmark-type data for developing more realistic high-resolution numerical models and simplified wake models for wind energy applications. The real-scale measurements from the abovementioned problems

can be combined with laboratory experiments to address scaling issues when extending laboratory measurements to field scale scenarios, and develop strategies to simulate full-scale dynamics under controllable laboratory conditions.

Acknowledgments This work was supported by US Department of Energy (grant No: DE-EE0002980) and the resources provided by the University of Minnesota College of Science and Engineering, Department of Mechanical Engineering and St. Anthony Falls Laboratory as part of the start-up package of Jiarong Hong.

References

- Adrian RJ (1991) Particle-imaging techniques for experimental fluid mechanics. *Ann Rev Fluid Mech* 23:261–304
- Adrian RJ (2005) Twenty years of particle image velocimetry. *Exp Fluids* 39:159–169
- Adrian RJ, Westerweel J (2011) Particle image velocimetry. Cambridge Univ. Press, Cambridge
- Adrian RJ, Meinhart CD, Tomkins CD (2000) Vortex organization in the outer region of the turbulent boundary layer. *J Fluid Mech* 422:1–54
- Aitken ML, Rhodes ME, Lundquist JK (2012) Performance of a wind-profiling lidar in the region of wind turbine rotor disks. *J Atmos Ocean Technol* 29:347–355
- Aydin K, Singh J (2004) Cloud ice crystal classification using a 95-GHz polarimetric radar. *J Atmos Ocean Technol* 21:1679–1688
- Barthelmie RJ, Larsen GC, Frandsen ST et al (2006) Comparison of wake model simulations with offshore wind turbine wake profiles measured by sodar. *J Atmos Ocean Technol* 23:888–901
- Barthelmie RJ, Hansen K, Frandsen ST et al (2009) Modelling and measuring flow and wind turbine wakes in large wind farms offshore. *Wind Energy* 12:431–444
- Bosbach J, Kühn M, Wagner C (2009) Large scale particle image velocimetry with helium filled soap bubbles. *Exp Fluids* 46:539–547
- Brandes E, Ikeda K, Zhang G et al (2007) A statistical and physical description of hydrometeor distributions in Colorado snowstorms using a video disdrometer. *J Appl Meteorol Climatol* 46:634–650
- Clifton A, Manes C, Rüedi J et al (2008) On shear-driven ventilation of snow. *Bound Layer Meteorol* 126:249–261
- Crowe CT, Schwarzkopf JD, Sommerfeld M et al (1998) Multiphase flows with droplets and particles. CRC Press, Boca Raton
- Genthon C, Town MS, Six D et al (2010) Meteorological atmospheric boundary layer measurements and ECMWF analyses during summer at Dome C, Antarctica. *J Geophys Res: Atmos* 115:D05104
- Handorf D, Foken T, Kottmeier C (1999) The stable atmospheric boundary layer over an Antarctic ice sheet. *Bound Layer Meteorol* 91:165–189
- Hanesch M (1999) Fall velocity and shape of snowflakes. Dissertation, Swiss Federal Institute of Technology, Zürich
- Hickson P, Carlberg R, Gagne R et al (2010) Boundary layer seeing measurements in the Canadian High Arctic. *Proc SPIE* 77331R:1–11
- Hobbs P, Chang S, Locatelli J (1974) The dimensions and aggregation of ice crystals in natural clouds. *J Geophys Res* 79:2199–2206
- Hong J, Katz J, Schultz MP (2011) Near-wall turbulence statistics and flow structures over three-dimensional roughness in a turbulent channel flow. *J Fluid Mech* 667:1–37
- Hosler C, Jensen D, Goldshlak L (1957) On the aggregation of ice crystals to form snow. *J Atmos Sci* 14:415–420
- Huang H, Dabiri D, Gharib M (1997) On errors of digital particle image velocimetry. *Meas Sci Technol* 8:1427
- Hutchins N, Chauhan K, Marusic I et al (2012) Towards reconciling the large-scale structure of turbulent boundary layers in the atmosphere and laboratory. *Bound Layer Meteorol* 145:273–306
- Jiménez J (2004) Turbulent flows over rough walls. *Annu Rev Fluid Mech* 36:173–196
- Justo JE, Bosworth GE (1971) Fall velocity of snowflakes. *J Appl Meteorol* 10:1352–1354
- Kaempfer T, Schneebeli M (2007) Observation of isothermal metamorphism of new snow and interpretation as a sintering process. *J Geophys Res: Atmos* 112:D24101
- Keane RD, Adrian RJ (1993) Theory of cross-correlation analysis of PIV images. In: Nieuwstadt FTM (ed) Flow visualization and image analysis. Kluwer Academic Publishers, Dordrecht, pp 1–25
- Langleben MP (1954) The terminal velocity of snowflakes. *Q J R Meteorol Soc* 80:174–181
- Lavoie P, Avallone G, De Gregorio F et al (2007) Spatial resolution of PIV for the measurement of turbulence. *Exp Fluids* 43:39–51
- Libbrecht KG (2005) The physics of snow crystals. *Rep Prog Phys* 68:855
- Maahn M, Kollias P (2012) Improved micro rain radar snow measurements using Doppler spectra post-processing. *Atmos Meas Tech* 5:2661–2673
- Manes C, Guala M, Egli L et al (2008) Statistical property of fresh snow roughness. *Water Resour Res* 44:W11407
- Matrosov SY (1993) Possibilities of cirrus particle sizing from dual-frequency radar measurements. *J Geophys Res: Atmos* 98:20675–20683
- Matrosov SY, Heymsfield AJ, Wang Z (2005) Dual-frequency radar ratio of nonspherical atmospheric hydrometeors. *Geophys Res Lett* 32:L13816
- Melling A (1997) Tracer particles and seeding for particle image velocimetry. *Meas Sci Technol* 8:1406–1416
- Metzger M, McKeon B, Holmes H (2007) The near-neutral atmospheric surface layer: turbulence and non-stationarity. *Philos Trans R Soc Lond Ser A* 365:859–876
- Mitchell DL, Heymsfield AJ (2005) Refinements in the treatment of ice particle terminal velocities, highlighting aggregates. *J Atmos Sci* 62:1637–1644
- Morris SC, Stolpa SR, Slaboch PE et al (2007) Near-surface particle image velocimetry measurements in a transitionally rough-wall atmospheric boundary layer. *J Fluid Mech* 580:319–338
- Musial W, Butterfield S, McNiff B (2007) Improving wind turbine gearbox reliability. In: Proceedings of the European wind energy conference NREL CP-50041548
- Nakiboğlu G, Gorré C, Horváth I et al (2009) Stack gas dispersion measurements with large scale-PIV, aspiration probes and light scattering techniques and comparison with CFD. *Atmos Environ* 43:3396–3406
- Raffel M, Willert CE, Wereley ST et al (2007) Particle image velocimetry: a practical guide, 2nd edn. Springer, Berlin
- Raupach M, Antonia R, Rajagopalan S (1991) Rough-wall turbulent boundary layers. *Appl Mech Rev* 44:1–25
- Stanislas M, Okamoto K, Kähler CJ, Westerweel J, Scarano F (2008) Main results of the third international PIV challenge. *Exp Fluids* 45:27–71
- Van Hout R, Zhu W, Luznik L et al (2007) PIV measurements in the atmospheric boundary layer within and above a mature corn canopy. Part I: statistics and energy flux. *J Atmos Sci* 64:2805–2824
- Vanderwende BJ, Lundquist JK (2012) The modification of wind turbine performance by statistically distinct atmospheric regimes. *Environ Res Lett* 7:034035

- Whale J, Anderson CG, Bareiss R et al (2000) An experimental and numerical study of the vortex structure in the wake of a wind turbine. *J Wind Eng Ind Aerodyn* 84:1–21
- White AB, Gottas DJ, Strem ET et al (2002) An automated brightband height detection algorithm for use with Doppler radar spectral moments. *J Atmos Ocean Technol* 19:687–697
- Wilson BM, Smith BL (2013) Uncertainty on PIV mean and fluctuating velocity due to bias and random errors. *Meas Sci Technol* 24:035302
- Zhang W, Wang Y, Lee SJ (2008) Simultaneous PIV and PTV measurements of wind and sand particle velocities. *Exp Fluids* 45:241–256
- Zilitinkevich S, Baklanov A, Rost J et al (2002) Diagnostic and prognostic equations for the depth of the stably stratified Ekman boundary layer. *Q J R Meteorol Soc* 128:25–46